Dirac magnons in honeycomb nanostructures

L. Giovannini [*]

Dipartimento di Fisica e Scienze della Terra, Università di Ferrara, Via G. Saragat 1, Ferrara I-44122, Italy

Magnon eigenmodes of an artificial structure consisting of cylindrical nanometric particles arranged in a honeycomb array are theoretically investigated, in zero applied field. The dispersion curves of the fundamental mode are calculated for two principal directions of the first Brillouin zone. A Dirac-like behavior, consisting of linear band crossing and zero-width gap, is found for moderate interdot separation. A tight-binding model fits the calculated behavior; the corresponding Dirac velocity has been obtained.

I. INTRODUCTION

After the discovery of unusual two-dimensional electronic excitations in graphene and of topological insulators [1], there has been a growing interest in materials, excitations, and structures that show analogous behaviors. The excitations of such systems, called Dirac materials, are well described by relativistic Dirac or Weyl equations. Silicene, gemanene [2], and stanene [3] are honeycomb lattice materials that have been proposed as alternatives to graphite to achieve an experimentally measurable quantum spin Hall effect; other nonhoneycomb lattice structures and materials have also been considered, as HgTe/CdTe quantum wells [4]. Although the majority of the discussion has focused on electrons, other excitations can show a Dirac-like spectrum, i.e., linear band crossing, gapless or with a small gap. They include excitations with Bose-Einstein statistics, such as phonons [5], photons [6], plasmons [7], and magnons [8–12].

Magnons are attractive as information carriers and in magnonic data processing because of the energy efficiency that can be achieved by avoiding the Joule effect that affects devices traditionally operated by electrons. In the gigahertz frequency regime where magnonic devices operate, the excitation wavelength is of the order of tens or hundreds of nanometers, allowing the spin-wave control by properly shaped artificial nanostructures, i.e., magnonic crystals, providing a large degree of freedom in manipulation. These nanostructures assume the form of periodic networks of magnetic nanoelements and are intensively studied [13]. While artificial nanostructures have already been studied as Dirac materials for plasmons [7], photons [6,14], and Cooper pairs [15], the behavior of Dirac magnons in artificial nanostructures is largely unexplored. The possibility of making honeycomb arrays of magnetic circular nanodots has been demonstrated, but the investigation was limited to long wavelength excitations ($k = 0$), without obtaining the dispersion curves [16].

The aim of this paper is to present a theoretical investigation of the spin eigenmodes of an artificial structure consisting of low cylindrical nanometric particles arranged in a honeycomb array, in zero applied field. The theory is based on a dynamical matrix approach which takes into account dipolar and exchange contributions, within a Bloch-wave expansion of the magnetization variables. When the dot separation is moderate and therefore the interdot interaction small, the collective modes can be well described by a tight-binding model. The frequency-wave vector dependence is investigated along two principal directions, and a Dirac-like behavior is found close to the K point of the first Brillouin zone.

II. SAMPLE GEOMETRY AND MAGNETIC PROPERTIES

The nanostructure investigated is shown in Fig. 1; it consists of an infinite two-dimensional artificial honeycomb lattice of ferromagnetic cylindrical dots placed on a nonmagnetic substrate. The cylindrical dot radius is $a = 50$ nm, height 20 nm; several values for the nearest-neighbor distance d are considered.

This structure can be described as a hexagonal Bravais lattice with a basis consisting of two identical but topologically inequivalent sites A and B, as shown in Fig. 2, where the primitive vectors $\mathbf{a}_1$ and $\mathbf{a}_2$ are also shown. The corresponding first Brillouin zone is shown in the right part of Fig. 2, with its principal points and the primitive vectors of the reciprocal lattice $\mathbf{b}_1$, $\mathbf{b}_2$.

For this simulation, Permalloy was chosen as the magnetic material, since artificial nanostructures are often experimentally made with this well-known material; furthermore, it has such small anisotropies that they can be neglected, thus preserving the spatial symmetries of the structure. It must be emphasized that the hexagonal symmetry is one of those which allow the realization of a Dirac material, and in many cases its breakage, due, for example, to magnetic anisotropies, leads to the destruction of the Dirac points [17,18]. The magnetic parameters are saturation magnetization $M_s = 800 \times 10^3$ A/m, exchange constant $A = 13.0 \times 10^{-12}$ J/m, and gyromagnetic ratio $\gamma = 185$ rad GHz/T. Damping is not included, as we focus on the determination of stationary states and
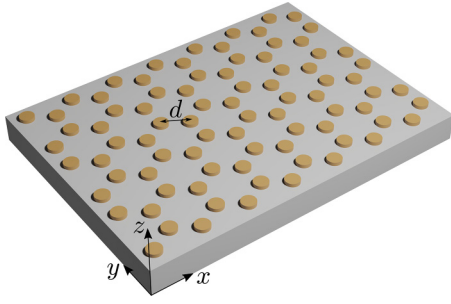
_____
[*]giovannini@fe.infn.it

FIG. 1. Sample geometry. A finite portion of the periodic two-dimensional lattice is represented, together with the reference frame used in the text.
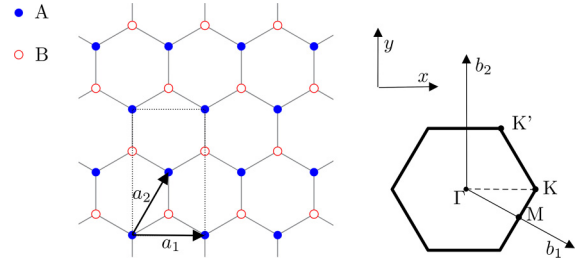

FIG. 2. Honeycomb lattice with primitive vectors $\mathbf{a}_1 = \sqrt{3}d\hat{x}$, $\mathbf{a}_2 = d/2(\sqrt{3}\hat{x} + 3\hat{y})$ (left), and first Brillouin zone with primitive vectors $\mathbf{b}_1 = \frac{2\pi}{3d}(\sqrt{3}\hat{x} - \hat{y})$, $\mathbf{b}_2 = \frac{4\pi}{3d}\hat{y}$ (right).

the corresponding magnonic band structure rather than on transport properties of the magnonic crystal.

III. MICROMAGNETIC CALCULATIONS

Due to the nanometric size of the structure, the position-dependent magnetization must be evaluated with a spatial resolution smaller than the exchange length. The magnetization ground state and its dynamics in a single nanostructure (the basis, that in our case consists of two cylindrical dots A and B) can be determined with numerical approaches, based on the discretization of the particle in space, i.e., its partition into a large number N of identical cells (finite-difference method). The normalized magnetization in each cell i, $\mathbf{M}_i$, can be written as the sum of a static and a (small) dynamic term perpendicular to the static one:

$$\mathbf{M}_i = \mathbf{M}_{0i} + \mathbf{m}_i. \tag{1}$$

Several micromagnetic packages are available for the calculation of the static magnetization $\mathbf{M}_0$; in the following, we use OOMMF 1.2β4 [19], which also includes periodic boundary conditions. When dealing with an infinite lattice, made of periodic repetitions of the basis, the interactions between different bases must be taken into account. For the ground-state calculation, the magnetization of all bases can be assumed identical so that the number of independent vector variables remains N.

A method based on the magnetization dynamical matrix of the system is then exploited for studying the magnetization dynamics [20]; in the following, it is briefly outlined. With this approach, the Landau-Lifshitz equation for the magnetization [21],

$$-\frac{1}{\gamma}\frac{\partial \mathbf{M}}{\partial t} = \mathbf{M} \times \mathbf{H}_{\text{eff}}, \tag{2}$$

is linearized and solved in $\mathbf{m}$. The effective field takes into account the dipolar and exchange contributions,

$$\mathbf{H}_{\text{eff}} = \mathbf{h} + \frac{2A}{M_s}\nabla^2\mathbf{m}; \tag{3}$$

here $\mathbf{h}$ is the dynamic dipolar field, there is no Zeeman interaction because we consider the case of no externally applied magnetic field, and Gilbert attenuation is neglected. Note that, while the exchange interaction is actually needed to properly

describe the inner magnetization of each dot (together with the dipolar one), the interdot interaction only occurs through the dipolar term because the disks are not in contact. Equation (3) is then written as a system of $2N$ linear equations in the $2N$ discretized variable components [20]. In particular, $\mathbf{h}$ is related to the magnetization distribution through the demagnetizing tensor $\overleftrightarrow{N}$:

$$\mathbf{h}_i = \frac{M_s^2}{2}\sum_{j=1}^{N}\overleftrightarrow{N}(j,i)\mathbf{m}_j. \tag{4}$$

In order to extend this approach to an infinite lattice, the dynamic magnetization and field are written in the Bloch form [22],

$$\mathbf{m}(\mathbf{r} + \mathbf{R}) = e^{i\mathbf{k}\cdot\mathbf{R}}\mathbf{m}(\mathbf{r}) \tag{5}$$

$$\mathbf{h}(\mathbf{r} + \mathbf{R}) = e^{i\mathbf{k}\cdot\mathbf{R}}\mathbf{h}(\mathbf{r}), \tag{6}$$

where $\mathbf{R} = n_1\mathbf{a}_1 + n_2\mathbf{a}_2$, $n_1, n_2 \in \mathbb{Z}$, and $\mathbf{k}$ is a Bloch wave vector; the effective fields of Eq. (3) are extended to include the interactions between cells belonging to different bases. This allows the numerical solution of Eq. (2) in a closed form, keeping the number of independent vector variables equal to N. For each eigenmode, the frequency f and magnetization profile $\mathbf{m}(\mathbf{r})$ are thus determined. Due to the finite accuracy with which the demagnetizing tensor is calculated iteratively and other roundoff errors, the calculated frequencies are affected by an error of ± 0.003 GHz. For each $\mathbf{k}$, calculating the eigenmodes takes about 2 hours on an 8-core Intel Xeon server.

Although a hexagonal Bravais lattice has a basis with different symmetry than a rectangular one, which is that used by both the OOMMF software and dynamical matrix method to implement the two-dimensional (2D) periodicity, it is possible to work around this problem by mapping the hexagonal lattice into a rectangular Bravais lattice, with a rectangular basis of double size (shown with dotted lines in Fig. 2) [23]. Therefore the calculated dispersion curves result folded in the halved first Brillouin zone and must be manually unfolded to recover the dispersion in the original symmetry. In the following, this procedure is carried out implicitly; the results are discussed directly in the hexagonal lattice in order not to complicate the presentation.
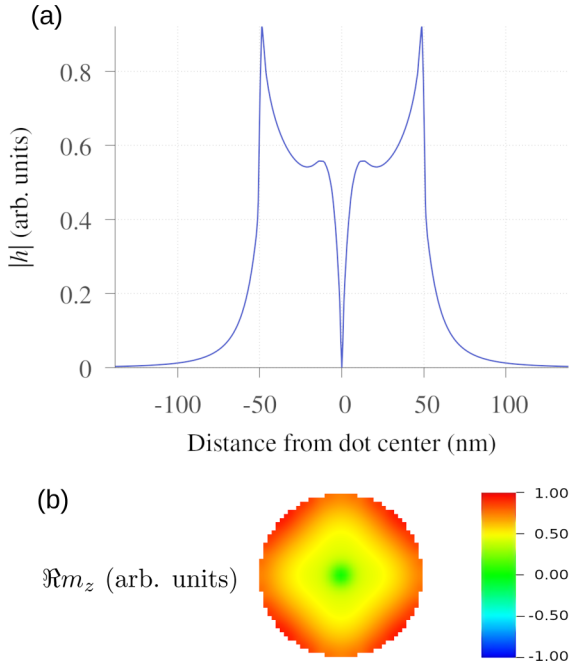
(a)

(b)

$\Re m_z$ (arb. units)

FIG. 3. Fundamental mode of an isolated dot, $f = 15.114$ GHz. (a) Dependence of $|h|$ on the radial coordinate. (b) Contour plot representing the position-dependent real part of m_z.

IV. RESULTS AND DISCUSSION

For values of the nearest-neighbor distance d ranging from 140 to 260 nm, the ground state and the spectrum of eigenmodes of the honeycomb structure are calculated. The micromagnetic cell is a $2.5 \times 2.5 \times 20$ nm size rectangular parallelepiped; in a basis (two magnetic cylinders) there are $N = 2528$ active cells. Since we assume no applied field, in the ground state the magnetization forms a vortex; clockwise direction and core pointing up are chosen. While in well-separated dots the magnetization is circularly symmetric, for smaller values of d the interdot interaction introduces a slight deformation, calculated and properly taken into account.

The eigenmodes of a cylindrical dot in the vortex ground state, apart from the gyrotropic mode, can be labeled with two integer indices (r, l), where the radial number r counts the circular nodal lines and the azimuthal number l corresponds to a phase shift of $2\pi l$ along a circular line [24]. We will mainly focus on the behavior of the fundamental $(0,0)$ mode because it has a nonvanishing average dynamic magnetization, thus giving rise to significant interdot interactions. Figure 3 shows the profile of the dynamic magnetization and field of the $(0,0)$ mode of a single dot for $d \to \infty$, i.e., when there is no interdot coupling. Apart from the factitious fourfold symmetry, due to creating the disk out of square-based parallelepiped cells [25–27], one can see that the dynamic field extends significantly beyond the edge of the dot, and this is the cause of interdot coupling and the appearance of collective modes of the artificial lattice.

Similarly to what happens to electrons in solids when the atomic wave functions overlap, as d becomes smaller and comparable with the dot size the degeneracy is progressively removed and a magnonic band opens. Actually, in a honey-
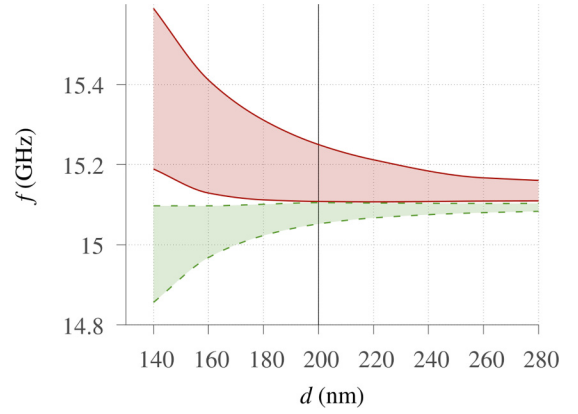

FIG. 4. Frequency dependence of the collective acoustical (solid red line) and optical (dashed green line) $(0,0)$ modes on the separation d. For each d the modes span a frequency interval (band).

comb lattice, the fundamental spin mode gives rise to two bands, acoustical and optical, according to the relative phase of the magnetization in sites A and B; they are shown in Fig. 4. The frequency is always lower for the optical mode, because interdot dipolar interaction favors (lower frequency) opposite magnetizations. For finite d the frequency of collective modes of each kind extends over a band as the Bloch wave vector k varies. For the separation marked with a vertical line in Fig. 4, $d = 200$ nm, the acoustical and optical bands are plotted in Fig. 5 along two principal directions. These curves show a peculiar behavior near the K point of the Brillouin zone, where the two bands approach each other to form a gap of zero amplitude (within the error affecting the numerical simulation). Moreover, close to K the curves effectively exhibit a linear behavior. These are distinctive markings of Dirac-like collective excitations. The bands calculated along ΓK' are identical (within the calculation error) to those calculated along ΓK and are not shown. A pseudospin index could then be introduced to represent the two Dirac states around K and K' [28], with a degeneracy that can be broken, for example, by boundary conditions or an asymmetric perturbative potential. Also, an in-plane external field may break the degeneracy (due
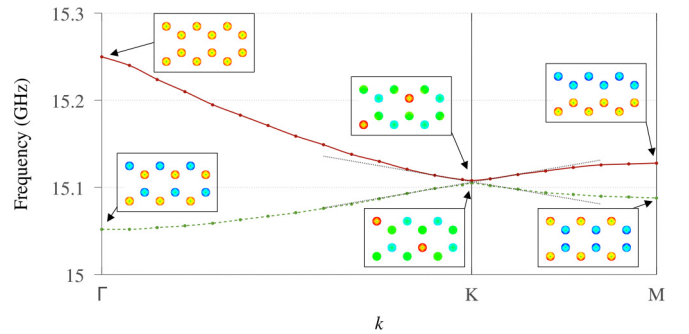

FIG. 5. Band diagram of the acoustical (solid red line) and optical (dashed green line) $(0,0)$ modes at $d = 200$ nm. Calculated frequencies (dots); lines are a guide for the eye. The dotted lines correspond to the fitted Dirac velocity. The insets are contour plots showing the real part of m_z in a portion of the infinite lattice, for some significant cases; the color scale is the same as Fig. 3.

to the fact that Damon-Eshbach-like modes do not have time-reversal symmetry), giving rise to intriguing effects; however, the bosonic nature of the excitations treated here and the unboundedness of the system seem to exclude the interesting effects that are produced at the Fermi energy in other systems by magnetic external fields, such as the integer or fractional quantum Hall effect [29].

A deeper insight can be gained by using a tight-binding approximate model to interpret these results. The motion equation can be mapped to a single orbital tight-binding Hamiltonian [8,17],

$$H = \epsilon \sum_i (a_i^\dagger a_i + b_i^\dagger b_i) - \hbar t \sum_{\langle ij \rangle} (a_i^\dagger b_j + a_i b_j^\dagger), \quad (7)$$

where the operators a_i and b_i destroy a magnon at the site i in the A and B sublattice, respectively. Here ϵ is the on-site hopping energy (diagonal term), $\hbar$ the reduced Planck constant, and t the transition rate between the A and B sites. The first term, with the summation running over the Bravais hexagonal lattice, describes the on-site magnon energies; the second, with the summation running over nearest-neighbors, describes the coupling between sublattices A and B. In reciprocal space Eq. (7) becomes

$$H = \sum_{\mathbf{k}} [\epsilon(a_{\mathbf{k}}^\dagger a_{\mathbf{k}} + b_{\mathbf{k}}^\dagger b_{\mathbf{k}}) + \Phi(\mathbf{k})a_{\mathbf{k}}^\dagger b_{\mathbf{k}} + \Phi^*(\mathbf{k})a_{\mathbf{k}} b_{\mathbf{k}}^\dagger], \quad (8)$$

where $a_{\mathbf{k}}$ and $b_{\mathbf{k}}$ are the Fourier transform of a_i and b_i, respectively, and Φ a structure factor depending on nearest-neighbor vectors. Around the K point, also called Dirac point, the wave vector can be expanded as $\mathbf{k} = \mathbf{K} + \mathbf{q}$; the eigenvalues are

$$\omega_\pm(\mathbf{q}) = \frac{\epsilon}{\hbar} + v_D|\mathbf{q}|, \quad (9)$$

with

$$v_D = \pm 3dt/2 \quad (10)$$

the Dirac velocity. Equation (9) expresses the essence of the behavior of a Dirac material, and is well suited to describe the dispersion curves found for $d = 200$ nm. A linear regression of the calculated frequencies around the Dirac point ($k = 1.2092 \times 10^7 \pm 1.51 \times 10^6$ m^{-1}), towards both the Γ and M directions, shows that the two slopes, positive and negative, are very close in modulus, $v_D = 37.98 \pm 2.43$ m/s and $v_D = -38.07 \pm 2.20$ m/s (with the standard error obtained from the regression). The bands appear substantially symmetric with respect to frequency inversion close to the K point, which supports the fact that the interaction between second nearest neighbors is negligible [28]. Figure 5 shows (dotted lines) the two straight lines corresponding to $v_D = \pm 38$ m/s. With this value, the transition rate between the A and B sites of the honeycomb lattice turns out to be $t = 0.127$ GHz; moreover, $f_0 = \epsilon/h = 15.107$ GHz, very close to the noninteracting dot fundamental frequency.

This picture no longer applies if the interdot interaction becomes too large. Figure 6 gathers the (0,0) bands calculated for d ranging from 140 to 260 nm (with the wave vectors related to each of the Brillouin zone sizes in order to be able to compare the curves). For $d \leqslant 180$ nm, i.e., $d/a \leqslant 3.6$, a noticeable gap opens at the K point, indicating that the results of the simplified tight-binding model introduced above no
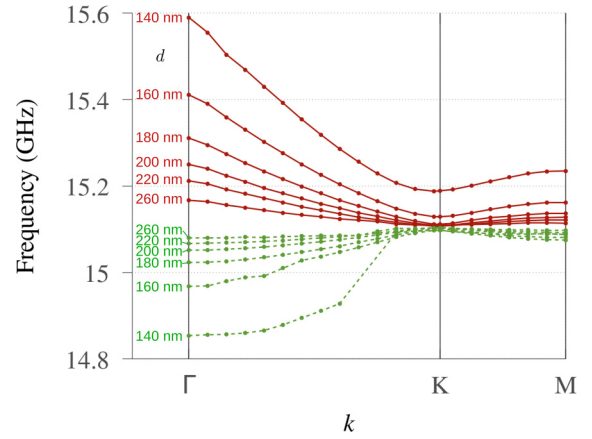

FIG. 6. Band diagram of the acoustical (solid red line) and optical (dashed green line) (0,0) modes for $d = 140 \ldots 260$ nm. Calculated frequencies (dots); lines are a guide for the eye. For some k values the frequency of the $d = 140$ nm optical mode could not be calculated unambiguously due to its intersection with other resonances.

longer apply. This happens because the stray field generated by the (0,0) mode of different dots gives rise to excessive overlap, so that the assumptions of the tight-binding model are no longer satisfied. Indeed, in this case the profiles show a significant deformation with respect to the circular symmetry of the mode shown in Fig. 3.

The dependence of the Dirac velocity on the separation d is shown in Fig. 7; Dirac velocities have been obtained through the same fitting procedure described above for $d = 200$ nm. The implicit dependence of the transition rate t on the separation distance d dominates on the explicit factor d in Eq. (10), as t is proportional to the dipolar coupling between adjacent dots, which in turns is inversely proportional to the cube of the distance, at not too small distances. Therefore for $d \to \infty$ the transition rate tends to zero and so does the Dirac velocity; in this limit the collective behavior of spin waves fades, the spin modes of different dots are no longer coupled, their frequencies degenerate, and the bands become
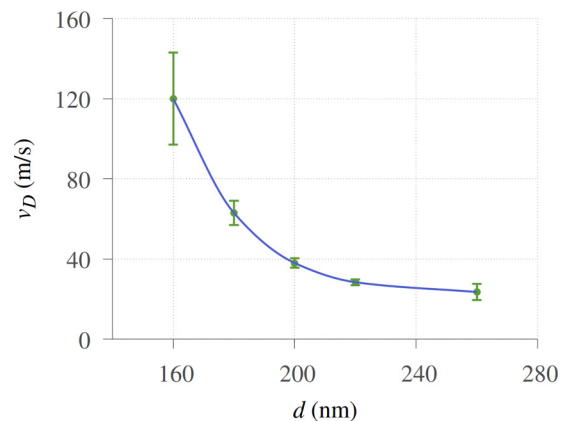

FIG. 7. Dirac velocity of the (0,0) mode as a function of d, found through a linear fitting close to the K point. The vertical bars represent the standard deviation, the line is a guide for the eye.
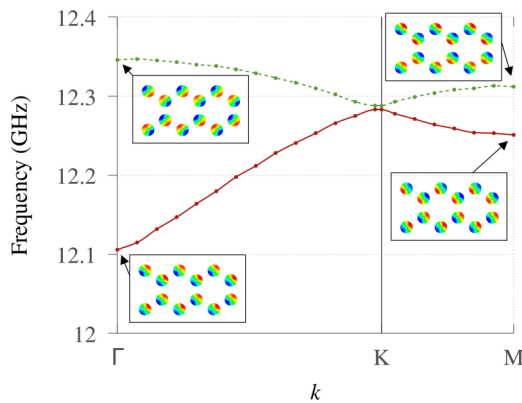
FIG. 8. Band diagram of the acoustical (solid red line) and optical (dashed green line) (0,1) modes at $d = 160$ nm. Calculated frequencies (dots); lines are a guide for the eye. The insets are contour plots showing the real part of m_z in a portion of the infinite lattice, for some significant cases; the color scale is the same as Fig. 3.
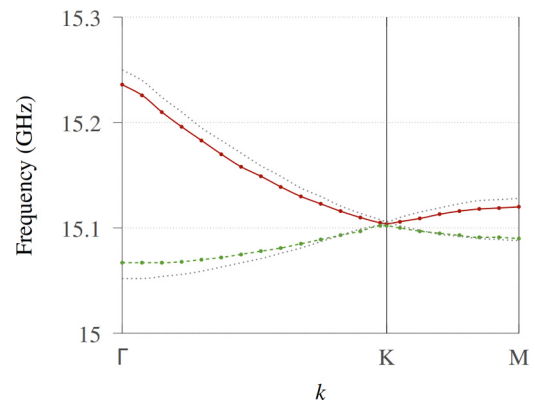

FIG. 9. Band diagram of the acoustical (solid red line) and optical (dashed green line) (0,0) modes at $d = 200$ nm for a system with alternated chirality between A and B sublattices. Calculated frequencies (dots); lines are a guide for the eye. The bands of the system with uniform chirality (taken from Fig. 5) are also shown for comparison (gray dotted lines).

flat. For the opposite case, the limit is given by the fact that the tight-binding approach fails when the dots become too close, as discussed above. Other factors make it possible to increase the dipolar coupling, as increasing the dot volume or using a magnetic material with bigger M_s but the mentioned limits still hold. For a nanometric artificial crystal, the Dirac velocity remains in the range of tens of m/s; the important result that in graphene Dirac electrons make massless particle physics accessible at speeds 300 times slower than that of light [30] is thus further extended.

The field outside the dot decays with a characteristic length which depends on the effective wavelength of the excitation, and therefore on the mode kind (indices r, l) and dot size (radius a). For example, the effective wavelength for the mode (0,1) is half that of the (0,0) mode, and a Dirac-like behavior can be found for d as small as 160 nm; its bands are shown in Fig. 8. The two bands approach each other to form a gap of essentially zero amplitude; however, for this mode the overall band width is small due to its vanishing average magnetization, and for the same reason it is also difficult to detect experimentally; it is therefore of less interest. Note that in this case the dipolar interdot interaction favors (lowest frequency) the acoustic mode, for which two adjacent dots have opposite magnetizations facing each other.

Finally, the role of chirality, i.e., of the orientation of the direction of rotation with respect to the direction of the ground-state magnetization in the vortex core, has been investigated for $d = 200$ nm. The frequency of the spin modes of a dot does not depend on chirality; therefore, when the chirality is inverted in all dots, the calculated band diagram (not shown) remains exactly the same as in Fig. 5. More interestingly, the system appears robust with respect to the inversion of the chirality of dots B only, with the chirality of dots A unchanged and therefore opposite to that of dots B. Figure 9 shows the acoustical and optical bands calculated for this system with

alternating chirality. In this case the bands change slightly with respect to the system with uniform chirality (0.1% maximum), but the gapless Dirac behavior is maintained at the K point. In other words, the system is robust with respect to the perturbation. This can be understood in the light of the fact that at K point the two modes are each located in a sublattice (A or B), which has uniform chirality, and since it does not influence the frequency of the modes, both have the same frequency.

V. CONCLUSIONS

The dispersion curves of spin waves on a honeycomb artificial nanostructure have been calculated along two principal directions of the Brillouin zone. A Dirac-like trend has been found close to the K point for a moderate value of the interdot coupling. A model based on a tight-binding Hamiltonian is found to well describe the behavior of the collective mode dispersions, thus allowing the extraction of the main parameters of the model.

Since the interdot coupling is driven by the dipolar interaction (there is no exchange coupling between nontouching dots), these results can be generalized to some extent to disks of different size. Changing the dot radius mainly affects the dispersion curves through the different interdot coupling, in turn due to the variable extent of the stray field. Therefore, apart from the absolute frequency variation of the mode, the Dirac-like behavior should hold for the fundamental mode when the lattice parameter is greater than about three times the dot radius; within this limit the system is robust with respect to dot radius variations. The geometrical parameters of this model calculation have already been chosen among those accessible experimentally; the effects found appear interesting for the purpose of controlling the spin waves and are able to stimulate experimental studies.

[1] L. Kou, Y. Ma, Z. Sun, T. Heine, and C. Chen, J. Phys. Chem. Lett. **8**, 1905 (2017), and references therein.

[2] C.-C. Liu, W. Feng, and Y. Yao, Phys. Rev. Lett. **107**, 076802 (2011).

[3] Y. Xu, B. Yan, H.-J. Zhang, J. Wang, G. Xu, P. Tang, W. Duan, and S.-C. Zhang, Phys. Rev. Lett. **111**, 136804 (2013).

[4] B. A. Bernevig, T. L. Hughes, and S.-C. Zhang, Science **314**, 1757 (2006).

[5] F. Li, X. Huang, J. Lu, J. Ma, and Z. Liu, Nat. Phys. **14**, 30 (2018).

[6] A. B. Khanikaev, S. H. Mousavi, W.-K. Tse, M. Kargarian, A. H. MacDonald, and G. Shvets, Nat. Mater. **12**, 233 (2013).

[7] G. Weick, C. Woollacott, W. L. Barnes, O. Hess, and E. Mariani, Phys. Rev. Lett. **110**, 106801 (2013).

[8] J. Fransson, A. M. Black-Schaffer, and A. V. Balatsky, Phys. Rev. B **94**, 075401 (2016).

[9] S. S. Pershoguba, S. Banerjee, J. C. Lashley, J. Park, H. Ågren, G. Aeppli, and A. V. Balatsky, Phys. Rev. X **8**, 011010 (2018).

[10] M. Malki and G. S. Uhrig, Europhys. Lett. **132**, 20003 (2020).

[11] Z.-X. Li, Y. Cao, and P. Yan, Phys. Rep. **915**, 1 (2021).

[12] A. Scheie, P. Laurell, P. A. McClarty, G. E. Granroth, M. B. Stone, R. Moessner, and S. E. Nagler, Phys. Rev. Lett. **128**, 097201 (2022).

[13] M. Krawczyk and D. Grundler, J. Phys.: Condens. Matter **26**, 123202 (2014).

[14] T. Ma, A. B. Khanikaev, S. H. Mousavi, and G. Shvets, Phys. Rev. Lett. **114**, 127401 (2015).

[15] S. Banerjee, J. Fransson, A. M. Black-Schaffer, H. Ågren, and A. V. Balatsky, Phys. Rev. B **93**, 134502 (2016).

[16] S. Saha, R. Mandal, S. Barman, D. Kumar, B. Rana, Y. Fukuma, S. Sugimoto, Y. Otani, and A. Barman, Adv. Funct. Mater. **23**, 2378 (2013).

[17] J. Cayssol, C. R. Phys. **14**, 760 (2013).

[18] L. Yan, M. Hua, Q. Zhang, T. U. Ngai, Z. Guo, T. C. Wu, T. Wang, and N. Lin, New J. Phys. **21**, 083005 (2019).

[19] M. J. Donahue and D. G. Porter, *OOMMF User's Guide, Version 1.0*, Interagency Report NISTIR 6376 (National Institute of Standards and Technology, Gaithersburg, MD, 1999).

[20] M. Grimsditch, L. Giovannini, F. Montoncello, F. Nizzoli, G. K. Leaf, and H. G. Kaper, Phys. Rev. B **70**, 054409 (2004).

[21] B. Hillebrands, Brillouin light scattering from layered magnetic structures, in *Light Scattering in Solids VII*, edited by M. Cardona and G. Güntherodt, Topics in Applied Physics Vol. 75 (Springer, Berlin, Heidelberg, 2000), p. 174.

[22] L. Giovannini, F. Montoncello, and F. Nizzoli, Phys. Rev. B **75**, 024416 (2007).

[23] A. Suzuki, M. Tanabe, and S. Fujita, J. Mod. Phys. **08**, 607 (2017).

[24] G. Carlotti, Appl. Phys. Rev. **6**, 031304 (2019).

[25] S. Mamica, J.-C. S. Lèvy, and M. Krawczyk, J. Phys. D: Appl. Phys. **47**, 015003 (2014).

[26] R. Wang and X. Dong, Appl. Phys. Lett. **100**, 082402 (2012).

[27] F. Montoncello, L. Giovannini, F. Nizzoli, R. Zivieri, G. Consolo, and G. Gubbiotti, J. Magn. Magn. Mater. **322**, 2330 (2010).

[28] A. H. Castro Neto, F. Guinea, N. M. R. Peres, K. S. Novoselov, and A. K. Geim, Rev. Mod. Phys. **81**, 109 (2009).

[29] N. M. R. Peres, F. Guinea, and A. H. Castro Neto, Phys. Rev. B **73**, 125411 (2006).

[30] A. C. Neto, F. Guinea, and N. M. Peres, Phys. World **19**, 33 (2006).